

# A finite element study of the deformations, forces, stress formations, and energy losses in sliding cylindrical contacts

Raghvendra Vijaywargiya, Itzhak Green\*

Georgia Institute of Technology, G. W. Woodruff School of Mechanical Engineering, Atlanta, GA 30332, USA

Received 24 January 2007; received in revised form 29 March 2007; accepted 29 March 2007

## Abstract

This work presents the results of a finite element analysis (FEA) used to simulate two-dimensional (2D) sliding between two interfering elasto-plastic cylinders. The material for the cylinders is modeled as elastic-perfectly plastic and follows the von Mises yield criterion. The FEA provides trends in the deformations, reaction forces, stresses, and net energy losses as a function of the interference and sliding distance between the cylinders. Results are presented for both frictionless and frictional sliding and comparisons are drawn. The effects of plasticity and friction on energy loss during sliding are isolated. This work also presents empirical equations that relate the net energy loss due to sliding under an elasto-plastic deformation as a function of the sliding distance. Contour plots of the von Mises stresses are presented to show the formation and distribution of stresses with increasing plastic deformation as sliding progresses. This work shows that for the plastic loading cases the ratio of the horizontal force to the vertical reaction force is non-zero at the point where the cylinders are perfectly aligned about the vertical axis. In addition, a “load ratio” of the horizontal tugging force to the vertical reaction force is defined. Although this is analogous to the common definition of the coefficient of friction between sliding surfaces, it just contains the effect of energy loss in plasticity. The values of the contact half-width are obtained for different vertical interferences as sliding progresses.

© 2007 Elsevier Ltd. All rights reserved.

*Keywords:* Cylinders; Finite element analysis; Frictional sliding; Frictionless sliding; Plasticity; Deformation; Stress; Reaction force; Energy loss

## 1. Introduction

Sliding contact between two elasto-plastic cylinders and spheres has important engineering applications in both the macro- and the microscale. The current results are normalized to be valid in both scales as long as continuum mechanics prevails. In microscale, it is well known that asperities deform plastically during sliding contact between rough surfaces. Thus, it is important to know the effect the contact has on the surface material and the geometry through plastic deformations and residual stresses. In macroscale, this information may be useful in analyzing the friction, wear, and deformation of contacts such as in gears, rolling element bearings, wheel on rail, when sliding may occur (in addition to rolling). In an electromagnetic launcher (EML) [1] an armature slides in a predefined spacing between two rails and, hence, this application

lends itself specifically to the boundary conditions used in the current work. The results presented here may also be valuable in analyzing human joints, such as that investigated by Chen et al. [2], wherein 2D plane strain finite elements are employed to model the temporomandibular joint using hyperelastic (Mooney–Rivlin) material. The approach is similar to the one taken in the current study only that here metallic-like material behavior is prevailing.

Both elastic and elastic–plastic spherical contacts have been analyzed in great detail in the last four decades. Predominantly considering normal loading only, a wide array of works have analyzed the contact of rough surfaces as reviewed by Liu et al. [3]. These works are based on the contact behavior of a single asperity in a statistical model of multiple asperity contact. All these works, share the common methodology of Thomas [4] and Greenwood [5] that is as follows:

- (1) Replacing the two rough surfaces by a smooth surface in contact with an equivalent rough surface.

\* Corresponding author. Tel.: +1 404 894 6779; fax: +1 781 846 0325.

E-mail address: [ithak.green@me.gatech.edu](mailto:ithak.green@me.gatech.edu) (I. Green).

**Nomenclature**

$b$	contact half width	$\Delta x$	total horizontal distance covered by the top cylinder to complete sliding
$C$	critical yield stress coefficient	$\delta x$	equal increments in which the total sliding horizontal sliding is covered
$E$	elastic modulus	$\nu$	Poisson's ratio
$E'$	equivalent modulus of elasticity, $\frac{1}{E'} = \frac{1-\nu_1^2}{E_1} + \frac{1-\nu_2^2}{E_2}$	$\sigma_e$	maximum equivalent von Mises stress
$F_x$	horizontal reaction force at the base of the bottom cylinder	$\omega$	interference between cylinder surfaces
$F_y$	vertical reaction force at the base of the bottom cylinder	$\omega^*$	non-dimensional vertical interference between cylinders, $\omega/\omega_c$
$i$	load step number	<i>Superscript</i>	
$L$	length of contact	*	dimensionless
$n$	number of load steps employed to simulate a quasi-static sliding process	<i>Subscripts</i>	
$P$	contact force	$c$	critical value at onset of plastic deformation
$P^*$	non-dimensional load, $P/P_c$	'	equivalent
$p_o$	maximum contact pressure	1	bottom cylinder
$R$	radius of the cylinder	2	top cylinder
$R$	equivalent radius, $\frac{1}{R} = \frac{1}{R_1} + \frac{1}{R_2}$	net	net value after sliding is completed
$S_y$	yield strength	res	residual value after sliding is completed
$U$	potential (strain) energy	$x$	corresponding to horizontal axis
$u$	maximum vertical displacement	$y$	corresponding to vertical axis
$x$	horizontal sliding distance covered by the top cylinder up to the $i$ th load step		

- (2) Replacing asperities with simple geometrical shapes.
- (3) Assume a probability distribution for asperity parameters.

Some of these works are restricted mainly to pure elastic regime, such as the landmark work by Greenwood and Williamson [6]. Other works, such as Greenwood and Tripp [7], Lo [8], Whitehouse and Archard [9], Tsukizoe and Hisakado [10], and Bush et al. [11,12], extend the Greenwood and Williamson model in the elastic regime to a variety of geometries and different basic assumptions. Other works concentrate on pure plastic deformation, and are based on the models of Abbott and Firestone [13] and Tsukizoe and Hisakado [10].

Normal spherical contacts in the elastic–plastic regime by Evseev et al. [14], Chang [15], and Zhao [16]. FEA has been used by Vu-Quoc et al. [17] to analyze contact between two spheres, which by symmetry is equivalent to that of one sphere in contact with a frictionless rigid plane, but the analysis is restricted to specific parameters and lack generality. Adams and Nosonovsky [18] provide a review on contact modeling with an emphasis on the forces of contact and their relationship to the geometrical, material and mechanical properties of the contacting bodies.

Recently, Jackson and Green [19], Wang and Keer [20], and Neliias et al. [21], have explored hemispherical elastic–plastic contact in normal loading. However, the characteristics of normal contact as opposed to sliding contact are quite different, and thus the latter is explored in this work. Hamilton and

Goodman [22] presented implicit equations and graphs of yield parameter and tensile stress distribution for circular sliding contact using the von Mises criterion for the prediction of yielding. Hamilton [23] further developed the implicit results in [22] to obtain explicit formulae for the stresses beneath a sliding, normally loaded Hertzian contact. However, these studies [22,23] concentrated on the effect of increasing friction in a sliding contact against a rigid flat, and on the resulting development of impending failure regions, but a coefficient of friction had a priori been imposed. In contrast, this work isolates the effects of purely frictionless sliding of interfering cylinders, and hence the development of stresses, energy loss, and other phenomena occur solely due to mechanical deformation. In [24] a dynamic analysis gives an estimation of the contact forces between wheels and rails in sliding. The analysis herein, is naturally related to such a line (or cylindrical) contact. Perhaps one of the earliest attempts in tackling interference sliding between two bodies (spheres) is that by Faulkner and Arnell [25], who quote extremely long execution times even for very coarse FEA meshes (~960 h for each simulation), leaving out generalization of the results. Steady-state dry frictional sliding between two elastic bodies by using Fourier series and integral transform techniques has been examined by Nosonovsky and Adams [26].

It is clear from the literature survey that a thorough investigation of the actual forces, deformations, stress formations, and most importantly energy losses due to plasticity for sliding in

the elastic–plastic regime is missing. The equivalent model of “elliptical contact against a rigid flat” is the consequence of the elastic Hertzian theory. Even though it had been used in normal elasto-plastic contact, such an “equivalent model” has no physical grounds or mathematical proof once plasticity takes place, certainly not when the two sliding bodies have distinct material properties. These parameters are particularly critical in understanding the sliding phenomenon under extreme conditions in an EML, and play a pivotal role in the design and construction of such systems. This work helps in understanding the aforementioned factors, thereafter the thermal and electromagnetic aspects of the problem can be amalgamated with these findings to form a comprehensive understanding of such sliding. In this work, elastic-perfectly plastic cylinders in sliding over each other are treated as whole bodies, and not as a part of a statistically generated surface. By means of FEA actual sliding is simulated, wherein the two interfering bodies are both fully modeled, without resorting to the common model of an equivalent body against a flat. This is particularly important when sliding takes place between dissimilar materials.

In the elastic domain and up to the onset of plasticity, the Hertzian solution [27] provides critical values of load, contact half-width, and strain energy. As explained by Green [28] and Jackson et al. [29], hardness is not implemented as a unique material property as it varies with the deformation itself as well as with other material properties such as yield strength, Poisson’s ratio, and the elastic modulus. Instead, the critical vertical interference,  $\omega_c$ , as derived by Green [28] for cylindrical contact, is employed. This quantity is derived by using the distortion energy yield criterion at the site of maximum von Mises stress by comparing the stress value with the yield strength,  $S_y$ . The critical values of force per unit length, half contact width, and interference are given as

$$\frac{P_c}{L} = \frac{\pi R(CS_y)^2}{E'}, \quad b_c = \frac{2R(CS_y)}{E'},$$

$$\omega_c = R \left( \frac{CS_y}{E} \right)^2 \left[ 2 \ln \left( \frac{2E'}{CS_y} \right) - 1 \right], \quad (1)$$

where

$$C = \frac{1}{\sqrt{1 + 4(v-1)v}}, \quad v \leq 0.1938,$$

$$C = 1.164 + 2.975v - 2.906v^2, \quad v > 0.1938. \quad (2)$$

The value of  $C$  is obtained from elasticity considerations, and the critical parameters are obtained at the point of yielding onset. To account for two different material properties note that  $CS_y = \min(C(v_1)S_{y1}, C(v_2)S_{y2})$ . The maximum elastic energy that can possibly be stored (up to the point of yielding onset) is used to normalize the net energy loss due to plastic deformation after sliding, and is likewise given by Green [28] as

$$\frac{U_c}{L} = \frac{\pi(CS_y)^4 R^2}{4E'^3} \left\{ 4 \ln \left[ \frac{2E'}{CS_y} \right] - 3 \right\}. \quad (3)$$

In this work, the critical values are calculated for a steel material with properties as follows:  $E_1 = E_2 = 200$  GPa, and  $\nu_1 = \nu_2 = 0.32$ . Since all the quantities are subsequently being normalized by the aforementioned Eqs. (1)–(3), the ensuing results apply for any geometry scale (as long as homogeneous and isotropic continuum mechanics prevails); therefore, the radii for the cylinders in the FE model are subjectively (and conveniently) chosen to be  $R_1 = R_2 = 1m$ . The above equations are expanded upon in the Appendix, and are likewise used to establish convergence of the finite element model.

### 1.1. Assumptions

Following are the assumptions that are used to simplify the problem:

- (1) The two cylinders are considered to be infinitely long in the direction perpendicular to sliding. This enables the FE model to be in 2D under the assumption of plane strain behavior.
- (2) The sliding bodies are idealized to have elastic-perfectly plastic behavior.
- (3) At first sliding is assumed to be a frictionless process, and hence no coefficient of friction is input in the FE model. This is done in order to isolate the effect of plasticity during sliding. Subsequently, this is relaxed and frictional sliding is investigated.
- (4) It is assumed that the mesh validated up to the onset of plasticity is also robust for analysis of the elastic–plastic regime, since no closed form solution is available beyond that point for this purpose.
- (5) Deformations in the bulk area are assumed not to have a significant bearing on the effects of sliding in the contact region. It is recognized that in contradiction to a point (hemispherical) contact problem, bulk deformation cannot entirely be neglected. However, this work concentrates on the area close to the contact surfaces and far field bulk deformation effects are assumed not to have a significant effect on the region close to the contact surfaces.
- (6) Sliding is simulated as a quasi-static process, i.e., time-dependent phenomena are not analyzed. Hence, dynamic effects are ignored and material properties used do not depend on the strain rate. Likewise, adhesion and stick-slip phenomena are not accounted for.
- (7) Temperature effects that occur due to sliding are not considered, and the material properties used are assumed to be at room temperature.

## 2. The finite element model

Two plane semi-circles representing the sliding cylinders are modeled and one is made to traverse over the other with a preset vertical interference  $\omega$  between the two (see Fig. 1). Sliding is simulated first as a frictionless process, i.e., no coefficient of friction is input in the FE model. Also, repeated sliding is not considered, and hence the top cylinder is made to pass over the bottom cylinder just once (i.e., ‘one-pass’ sliding).

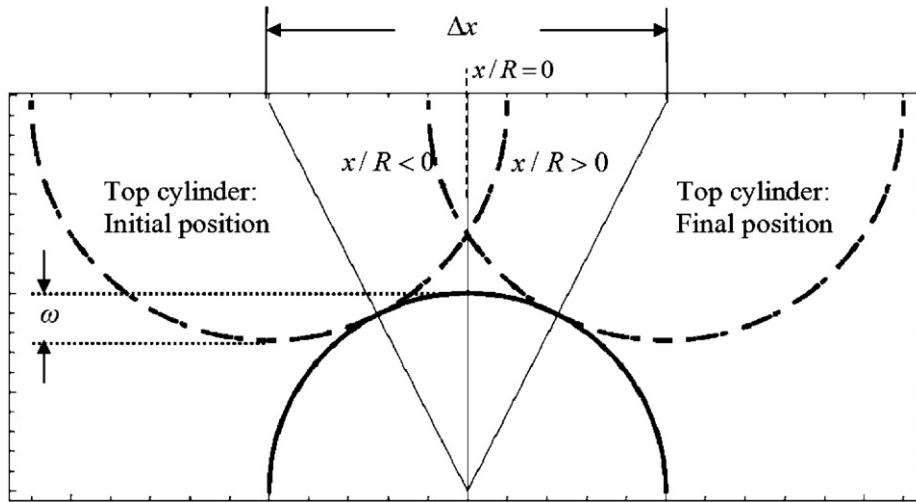


Fig. 1. Schematics of the sliding process.

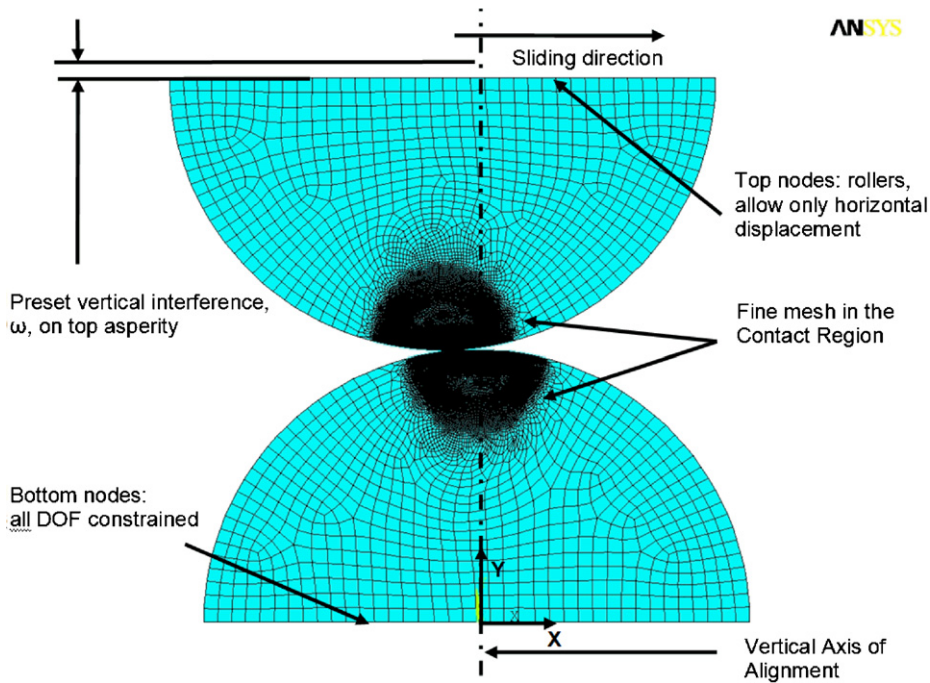


Fig. 2. Schematic of the FEA model for sliding between cylinders.

Sliding is attained piecewise as the top cylinder traverses a total displacement,  $\Delta x$  (see Fig. 1). This  $\Delta x$  is calculated from geometry and it is a function of the vertical interference,  $\omega$ , where naturally  $\Delta x$  increases with the preset interference  $\omega$ . That total distance is divided into  $n$  equal load steps,  $\delta x = \Delta x/n$ . Hence, at load step  $i$  the location of the center of the traversing cylinder relative to the center of the stationary cylinder is

$$x = i \cdot \delta x - \frac{\Delta x}{2}, \quad i = 0, n + m.$$

Because of material tugging  $m$  load steps are added to ensure exit from sliding contact.

Normalizing  $x$  by  $R$ , the loading phase is defined by the region  $x/R < 0$ , where the top cylinder is pressed horizontally against the bottom one before passing the vertical axis of alignment ( $x/R = 0$ ). The unloading phase is defined in the region  $x/R > 0$ , where the top cylinder has passed the vertical axis of alignment, and where the cylinders are expected to repel each other. The nodes at the base of the bottom cylinder (Fig. 2) are constrained from displacement in the  $X$  and  $Y$  directions. The nodes at the base of the top cylinder are also constrained from displacement in the  $Y$  direction, but are allowed to displace freely in the  $X$  direction upon sliding. The fixed horizontal sliding displacement is equally imposed on these nodes.

Table 1  
Validation of the meshing scheme employed

$\omega^*$	ANSYS $b(m)$	Theoretical $b(m)$	% diff	ANSYS $\sigma_e$ (GPa)	Theoretical $\sigma_e$ (GPa)	% diff	ANSYS $p_o$ (GPa)	Theoretical $p_o$ (GPa)	% diff
0.2	0.00663	0.00579	−14.3	0.338	0.355	4.8	0.615	0.646	4.7
0.3	0.00784	0.00726	−8.0	0.433	0.445	2.7	0.786	0.809	2.9
0.5	0.01010	0.00964	−4.8	0.585	0.591	1.0	1.058	1.074	1.5
0.7	0.01202	0.01162	−3.4	0.709	0.712	0.5	1.279	1.294	1.2
1.0	0.01445	0.01397	−3.4	0.858	0.856	−0.2	1.545	1.556	0.7

A reasonably large range of vertical interferences,  $\omega$ , coupled with horizontal sliding distance (from one side where the cylinders are just in contact to the other side where they just come out of contact), is used to simulate sliding.

To establish confidence in the mesh for different loading schemes (ranging from elastic to highly plastic), a 2D plane strain FEA simulation of the cylindrical line contact is performed. The modeling and meshing for this simulation is similar in approach to that employed by Jackson et al. [19,29]. However, instead of a quarter-circle and a rigid flat, contact in this case is between two elasto-plastic semi-circles representing the two cylinders. In addition, a new meshing scheme is introduced wherein a semi-circular dense region of elements is used to capture the high stresses in the small region of contact (see Fig. 2). In [19,29] a rectangular region is employed for the same purpose.

The commercial FEA software ANSYS® is used to perform the analyses. The mesh is constructed using eight node quadrilateral elements (Plane 82) and surface-to-surface contact elements (Contact 172 and Target 169). Once the predetermined regions are established, ANSYS is used to automatically mesh the said regions. Various mesh schemes are tried to achieve convergence. The optimized model has 83 372 nodes, 25 570 elements, and 200 contact elements in the region of interest.

The mesh is validated first for a purely aligned normal elastic contact (non-sliding), with  $S_y=0.856$  GPa, and results are compared against the analytical solution obtained by Green [28], as summarized in the Appendix. In this FEA model values of vertical interference,  $\omega$ , are imposed and numerical results are extracted for the contact half-width, the maximum von Mises stresses, and the maximum pressure (i.e.,  $p_e = |\Phi_z|$  at the axis of symmetry on the surface  $\zeta = |z/b| = 0$ ; see Eq. (11) in the Appendix). Corresponding to the imposed interferences,  $\omega$ , the theoretical values of  $P/L$  are solved from Eq. (13), the contact widths,  $b$ , are calculated from Eq. (9), the maximum von Mises stresses are calculated from Eqs. (10) and (12) at  $\zeta_m$ , and the  $p_o$  values are calculated from Eq. (8). The results of this validation are summarized in Table 1, where the last row represents the critical values at  $\omega = \omega_c$  (or  $\omega^* = \omega/\omega_c = 1$ ). For the interferences examined, the maximum disagreement between the FEA values and the theoretical values occurs at the lowest applied vertical interference of  $\omega^* = 0.2$ . The accord between the FEA and the theoretical values gets progressively better as higher vertical interferences approaching criticality are applied. The

contact half width,  $b_c$ , differs by only 3.4%, where the maximum equivalent von Mises stress,  $\sigma_e$ , and the maximum contact pressure,  $p_e$ , differ by less than 1%. The larger error in the contact half-width is attributed to the finite FEA grid, i.e., the resolution or spacing between the contact elements. The smaller the interference, the smaller number of contact elements are in effect, leading to a larger error, and vice versa. Noteworthy, for as long as  $\omega < \omega_c$  extremely good agreement is found also between the parameters calculated for sliding contact when the two cylinders are at vertical alignment compared to those for non-sliding normal contact (as it should).

For this non-linear problem, small load steps are used toward incremental (quasi-static) sliding from one end to the other. Values of the contact force, stress tensor, von Mises stress, and displacement are recorded at each load step. The contact forces are determined by summing the reaction forces at the base of the bottom cylinder.

In this analysis, sliding takes place under interference values sufficiently larger than the critical interference, and thus additional mesh convergence tests are now undertaken. As no closed-form solutions are available for the elastic–plastic domain with which the FE model can be validated, additional combinations of reasonable boundary conditions and meshing schemes are checked to attest the sliding results. These are all done at an intermediate interference value of  $\omega^* = 9$ , and results are compared against each other. The cases are as follows:

- To verify the meshing scheme employed, both the top and bottom cylinders are meshed such that the nodes and elements generated mirror each other across their respective axes of symmetry. This is different from the automated (default) meshing technique employed by ANSYS (described earlier), which generates a mesh that is not mirrored, and hence is not exactly symmetric. However, the results obtained via both approaches are practically identical.
- The employed boundary condition, wherein the bottom cylinder base is affixed and the top cylinder slid across, is checked against other equivalent boundary conditions. This is done by placing the nodes at the bases of both cylinders on rollers. Opposing horizontal displacements are then applied to the bases of both cylinders to simulate sliding. This procedure yields results that are identical to those presented in this paper.
- Instead of an 8-node quad element, a 6-node triangular element in a perfectly symmetric meshing is used on the case

where the two cylinders are slid against each other. Again, this resulted in no change in the intermediate load steps and the final results.

- Likewise, affixing the upper cylinder and sliding the bottom cylinder, with either meshing scheme, also produces identical results. That is, the upper cylinder and lower cylinder maintained their own stress and deformation patterns.

Noteworthy, the computational cost is considerably smaller when using the boundary conditions where displacement is applied to only one of the cylinders. Since all feasible combinations of boundary conditions and various meshing schemes produce indistinguishable results, the meshing scheme discussed first is upheld and used for the entire study. It is postulated that the FEA mesh used is trustworthy.

### 3. Results and discussion

The following results pertain to steel with  $S_y = 0.9115$  GPa, and they are presented for a range of preset normalized vertical interferences,  $\omega^*$ , from 1 (elastic limit) to 20 (elastic–plastic). The material properties used for the cylinders are chosen to be steel, which is commonly employed in many engineering applications. The computation time is about an hour for sliding with small vertical interferences to about 4 h for sliding with larger interferences on a dual processor Xeon 3 GHz PC with hyperthreading turned on to utilize four virtual processors.

#### 3.1. Deformation

Since both cylinders are modeled with the same material properties, the deformation pattern followed by the two is identical. The maximum vertical displacements,  $u_y$ , of the nodes on the cylinder surfaces are monitored in order to understand the deformation of the cylinders. The position of this maximum vertical displacement on the surface of the cylinders moves along as sliding progresses because of the curvature of the two cylinders. The value  $u_y$  is effectively normalized by the critical interference  $\omega_c$  given in Eq. (1). Plots of the normalized maximum vertical displacement,  $u_y/\omega_c$ , with respect to the normalized sliding distance of the top cylinder,  $x/R$ , are presented for a range of  $\omega^*$  varying from 1 (elastic limit) to 20 (elastic–plastic) in Fig. 3.

As expected, for  $\omega^* = 1$ , the vertical displacements are symmetric about the axis of alignment. Also, displacements increase with the increase in vertical interference  $\omega^*$ , i.e., with increase in load. It can be seen that for  $\omega^* > 1$ , there is plastic deformation in that the curves do not come back down to the zero displacement line, i.e., to the  $X$  axis. Instead, it flattens out and preserves the plastic deformation that has occurred as can be seen from the last few data points on each curve. This normalized vertical residual deformation,  $u_{res}/\omega_c$ , increases with the increase in vertical interference between the cylinders as shown in Fig. 3. Also, for  $\omega^* = 20$ , it is observed that the maximum vertical deformation actually occurs after the cylinders have

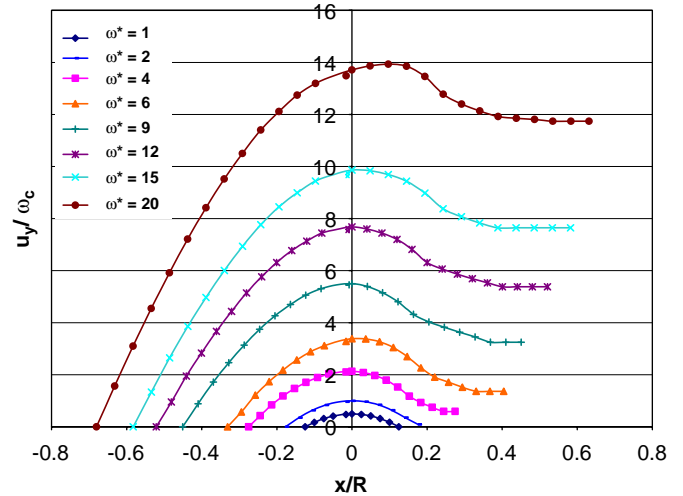


Fig. 3. Normalized maximum vertical displacement vs. normalized sliding distance.

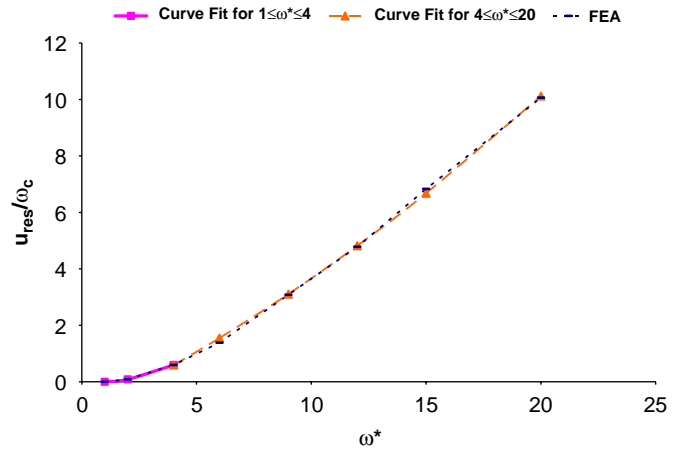


Fig. 4. Development of residual deformation with increase in vertical interference.

passed the vertical axis of alignment. This phenomenon can be attributed to material tugging and pile-up caused by large plastic deformation.

To capture the residual deformations the last point in Fig. 3 are extracted for different ranges of the applied vertical interference, and equations are fitted to the numerical data, as shown in Fig. 4:

$$\begin{aligned} \frac{u_{res}}{\omega_c} &= 0, & \omega^* \leq 1, \\ \frac{u_{res}}{\omega_c} &= 0.03045(\omega^* - 1) + 0.05556(\omega^* - 1)^2, & 1 \leq \omega^* \leq 4, \\ \frac{u_{res}}{\omega_c} &= 0.59139 + 0.47795(\omega^* - 4) \\ &\quad + 0.01391(\omega^* - 4)^2, & 4 \leq \omega^* \leq 20. \end{aligned} \tag{4}$$

These equations are continuous at  $\omega^* = 1$  and 4.

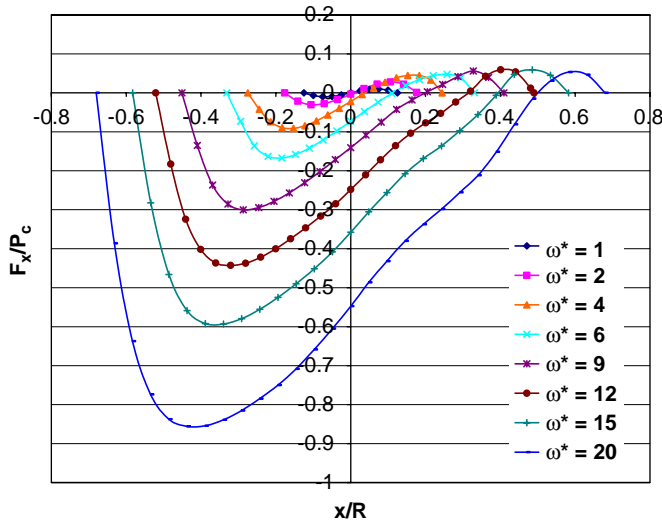


Fig. 5. Normalized horizontal reaction force vs. normalized sliding distance.

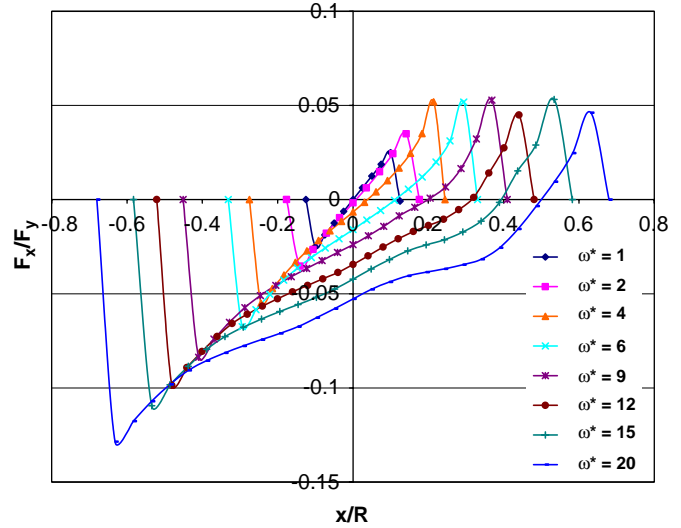


Fig. 7. “Load Ratio” vs. normalized sliding distance.

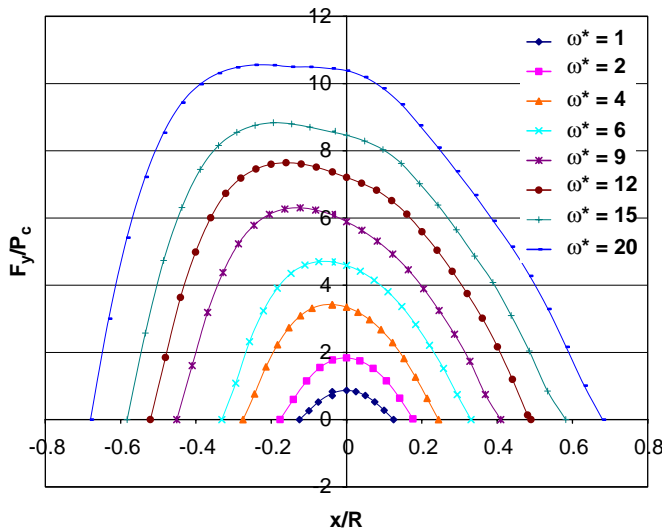


Fig. 6. Normalized vertical reaction force vs. normalized sliding distance.

### 3.2. Forces

Reaction forces at the base nodes of the bottom cylinder are summed for each load step and plotted against the normalized horizontal sliding distance  $x/R$ . Both the tangential reaction force,  $F_x$ , and the normal reaction force,  $F_y$ , are normalized by the critical load,  $P_c$  given in Eq. (1). Figs. 5 and 6 show the trends followed by  $F_x/P_c$  and  $F_y/P_c$ , respectively, as the top cylinder slides across the bottom one.

As expected, it is apparent that for the vertical interference  $\omega^* = 1$ , the curve is anti-symmetric in Fig. 5, and symmetric in Fig. 6, signifying no plasticity or loss of energy once sliding is completed. However, for the elastic–plastic loading cases, where  $\omega^* > 1$ , permanent plastic deformation occurs and some energy is lost in the process. This is evident from Fig. 5 as the area under (energy invested in sliding) is larger than that

above (energy restored in rebound) for all the curves in the elastic–plastic regime. This shows that more work is done in pushing the top cylinder across the bottom one in the loading phase, than what is earned once it has passed the vertical axis of alignment in the unloading phase where both cylinders are repelling each other. Also, it is apparent from Fig. 6 that the normalized vertical reaction force,  $F_y$ , is symmetric for  $\omega^* = 1$ , but becomes higher and increasingly skewed during loading than unloading as the applied vertical interference is increased. This may be attributed to predominantly elastic resistance during loading which diminishes once plasticity spreads in the contact.

Now, a “load ratio” is defined as  $F_x/F_y$ , being the ratio of the horizontal reaction force with respect to the vertical reaction force. This ratio is generated and plotted versus the normalized sliding distance as shown in Fig. 7. While each of the data points on these curves can be thought of as a quantity similar to the instantaneous local coefficient of friction, it is emphasized that this is not a “coefficient of friction” in the traditional sense since other effects (e.g., adhesion, contamination) are not accounted for. This load ratio applies only to this isolated mechanical sliding process. Moreover, in the region where the cylinders repel each other, the positive “load ratio” does not truly indicate a “negative coefficient of friction.”

For the elastic loading case of  $\omega^* = 1$ , the curve in Fig. 7 is (as expected) anti-symmetric. For the elastic–plastic loading cases with  $\omega^*$  ranging from 2 to 20, it can be seen that the maximum magnitude of the “load ratio” increases steadily as  $\omega^*$  increases. However, once the top cylinder has passed the vertical alignment axis and is repelling the bottom cylinder, the maximum “load ratio” magnitude does not vary much for the different  $\omega^*$  applications. This is evident from plot in Fig. 7. It is thus reasonable to postulate that for  $\omega^* \geq 4$ , the maximum “load ratio” in unloading becomes constant with a value of approximately 0.05. In addition, the plot clearly shows that for all vertical interferences, the magnitude of the “load ratio”

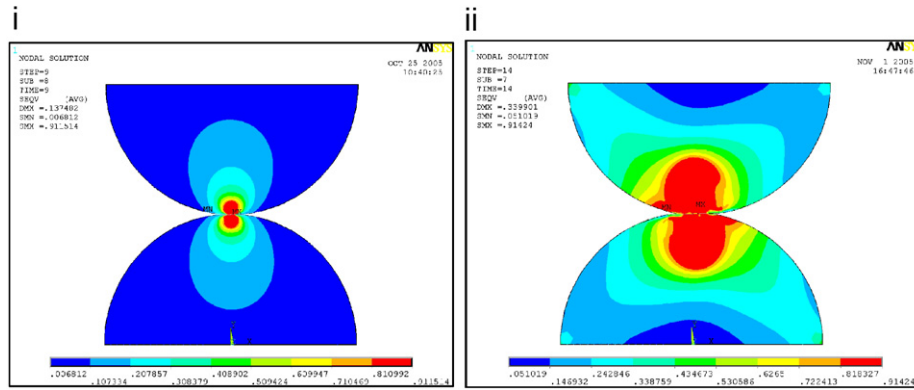


Fig. 8. von Mises stress contours for sliding cylindrical contact at vertical interferences of (i)  $\omega^* = 4$  and (ii)  $\omega^* = 20$  at the vertical axis of alignment.

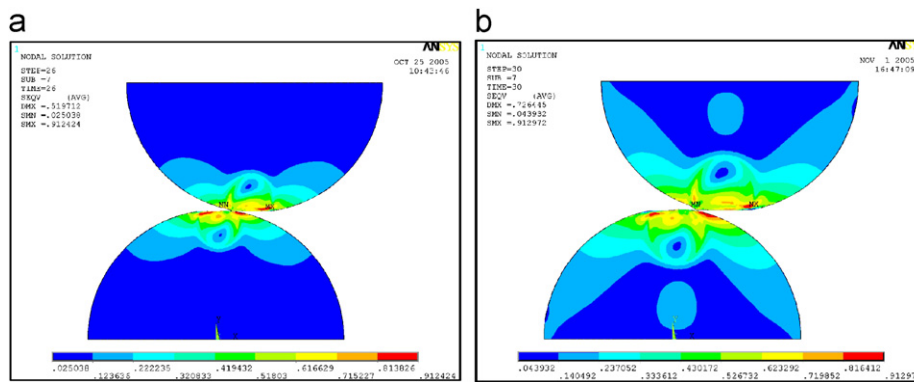


Fig. 9. Residual von Mises stress contours for sliding cylindrical asperities for (a)  $\omega^* = 12$ , (b)  $\omega^* = 20$ .

during elasto-plastic loading is always greater than that during unloading.

It is also clear from the plot that for the plastic loading cases, the ratio of the horizontal to the vertical reaction force is not zero at the point where the cylinders are perfectly aligned about the vertical axis. It is noteworthy from Figs. 5 and 7 that for sliding between cylinders, additional tangential load can be supported with increasing  $\omega^*$ , even if the contact interface has become plastic, where in fact the tangential load increases with the interference.

### 3.3. Stress formation

The stress regions formed in both cylinders are by and large anti-symmetric about the axis of alignment throughout the course of the sliding process, since identical material properties and geometries are used to model both cylinders. This holds for the elastic, as well as all of the elastic–plastic ranges. At low interferences, the high stress region develops below the contact interface. As sliding progresses and load on the cylinders increases for the elastic–plastic loading ranges, yielding occurs and a sub-surface plastic core develops (see Fig. 8). Elastic material surrounds this plastic core, and provides the greater part of resistance to sliding. As the load increases with the progression of sliding (i.e., rendering an increase in the

effective interference), the elastic region diminishes, making way for the growth and propagation of a plastic core, which diminishes the resistance to sliding.

At the vertical axis of alignment, as seen from Fig. 8, the von Mises stress distribution in both cylinders is mostly identical (in an anti-symmetric pattern), with regions of slightly higher concentrations in the direction of sliding signifying resistance to sliding. For lower elastic–plastic vertical interferences, such as  $\omega^* = 4$ , high stresses remain near the area of contact, i.e., there is no significant stress formation at the base of the cylinders (where they may be connected to a bulk material). As the vertical interference increases, however, stresses can be seen developing in the body of the cylinder as well as at the base (see Fig. 8). This signifies shear tugging at the cylinder base, and for vertical interference causing extreme plastic deformations, this might very well be the region with the highest stresses. This work concentrates on the elastic–plastic regime at the vicinity of contact, and hence only those results are expounded upon.

Fig. 9 shows the distribution of the residual stresses after sliding is completed for vertical interference values  $\omega^* = 12$  and 20. As expected, the residual stresses for the case with  $\omega^* = 20$  are more widely spread than those for  $\omega^* = 12$ . Some of these stresses remain at the yield value (i.e., residual plastic strain). Also, it can be seen that there are remnants of the stress in the



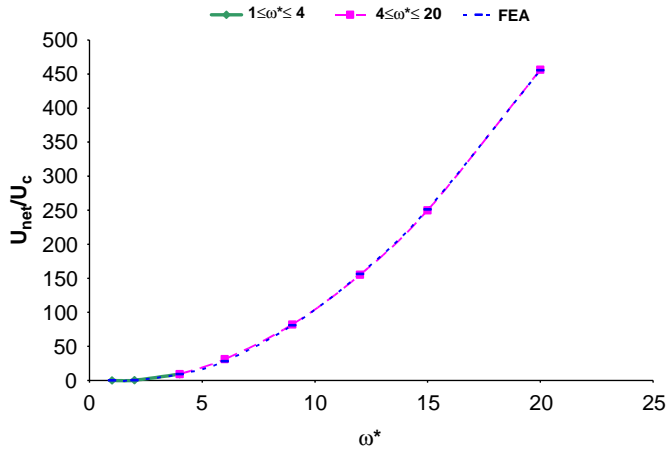


Fig. 10. Normalized energy loss vs. normalized vertical interference.

bulk of the cylinders away from the area of contact as well as at their bases. As discussed earlier, for highly plastic vertical interferences, this occurrence would become significant as the mode of failure might be the initiation of cracks or the shearing-off of the cylinders. This phenomenon is beyond the scope of this work and it is not explored herein.

3.4. Energy loss

Energy loss in sliding for individual preset vertical interference cases is separately calculated by evaluating the areas under each of their respective horizontal reaction curves in Fig. 5. This represents the net work done when sliding the top cylinder over the bottom. It is emphasized that because of the boundary conditions used herein, where the nodes at the bases of the two half cylinders do not translate in the Y direction, the reaction force  $F_y$  does not do work. The work done is solely due to  $F_x$ . The values obtained,  $U_{net}$ , are normalized by  $U_c$  from Equation (3). Fig. 10 shows the plot of  $U_{net}/U_c$  for each of the preset vertical interferences,  $\omega^*$ , as calculated from the FE simulations.

Second order polynomial curves are then fitted to the numerical data. They represent the trend followed by energy loss for different ranges of the applied vertical interference,  $\omega^*$ , and are found to closely capture the increasing energy loss with increasingly elastic–plastic loading. The fitted equations are as follows:

$$\begin{aligned} \frac{U_{net}}{U_c} &= 0, & \omega^* \leq 1 \\ \frac{U_{net}}{U_c} &= -9.487(\omega^* - 1) + 13.409(\omega^* - 1)^2, & 1 \leq \omega^* \leq 4 \\ \frac{U_{net}}{U_c} &= 92.221 + 85.238(\omega^* - 4) \\ &+ 12.133(\omega^* - 4)^2, & 4 \leq \omega^* \leq 20. \end{aligned} \tag{5}$$

These equations are continuous at  $\omega^* = 1$  and 4.

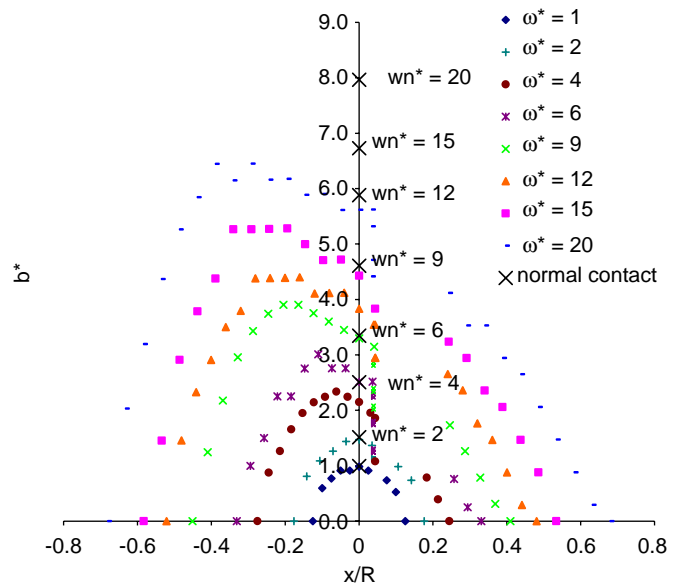


Fig. 11. Normalized contact half-width for each load step vs. normalized sliding distance.

3.5. Contact half-width

Fig. 11 shows the trend followed by the contact half-width,  $b$ , as it changes with each load step as sliding with different vertical interferences progresses. It is normalized by the critical contact half-width,  $b_c$ , and is hence plotted as the ratio  $b^*$ . It is observed that the contact half width curve for sliding with vertical interference  $\omega^* = 1$  is symmetric about the vertical axis of alignment where the cylinders are exactly on top of each other. As  $\omega^*$  increases, the curves get more and more skewed at the loading phase of the sliding process. Also in Fig. 11, the value of the contact half-width is given by the symbol ‘x’ for perfectly symmetric, normal contact simulation between the same cylinders, designated by  $\omega_n$ . For  $\omega^* = 1$ , as expected the contact half-widths for the sliding and normal loading cases is found to be the same. However, for interferences  $\omega^* \geq 1$ , the contact half-widths,  $b^*$ , for normal loading of cylinders are consistently higher than those for sliding interference at the vertical axis of alignment. This is because in normal loading material is flattened and flows equally sideways, while in sliding material is being tugged, flowing plastically away from the contact interface.

3.6. Frictional vs. frictionless sliding

In reality, sliding between any two surfaces is likely to contain friction. Friction plays an important, and in most cases pivotal, role in the behavior of surfaces as they slide over each other. Now that the part played by pure plastic deformation in elastic–plastic sliding has been analyzed, the next step is to see how friction combines with the aforementioned to affect the sliding process. This analysis is thus closer to the actual setting found in most applications, and hence a relatively common coefficient of friction of 0.3 is used for the purpose of the FEA.

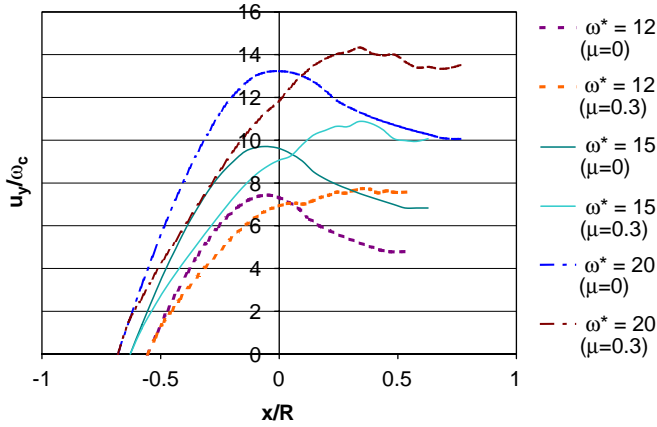


Fig. 12. Comparison of normalized maximum deformation plots for steel–steel sliding with and without friction.

This helps in highlighting the part played by each of the two aforementioned factors. The methodology employed for this analysis is the same as the approach used in the frictionless analysis, except that in this case a coefficient of friction is introduced between the two sliding cylinders to study the effect of friction in such sliding.

### 3.6.1. Deformations

Fig. 12 shows the plot of  $u_y/\omega_c$  vs.  $x/R$  for both the frictionless and frictional steel–steel sliding cases for the vertical interferences of  $\omega^* = 12, 15$ , and  $20$ . The peak deformations for  $\omega^* = 12$  are about the same, but while for the frictionless sliding case the deformation decreases after reaching the peak, for frictional sliding it increases marginally. For  $\omega^* = 15$  and  $20$ , the magnitudes of  $u_y/\omega_c$  are noticeably higher than those for the frictionless case. The resultant residual deformation magnitudes for frictional sliding cases are found to be significantly higher than those found in corresponding frictionless sliding cases. This is evident from the fact that in Fig. 12 curves for frictional sliding consistently finish higher than the corresponding frictionless curves.

### 3.6.2. Forces

Figs. 13 and 14 show a comparison of the plots of the normalized horizontal force and normalized vertical force for the frictionless and frictional sliding cases. Expectedly, none of the curves that are plotted for the frictional sliding cases show positive values. The peak values for both the frictionless as well as the frictional sliding cases lie before  $x/R = 0$ . Because of material pile-up in the cases of frictional sliding, the area under the horizontal reaction curve is much larger than that in the frictionless sliding cases. This signifies greater energy loss due to the presence of friction.

### 3.6.3. Stress formations

Fig. 15 captures the von Mises stress contours found in frictionless and frictional sliding analyses. The most significant difference in the stress contours of these two cases is the axis of symmetry for the stress pattern. For both frictionless as well as

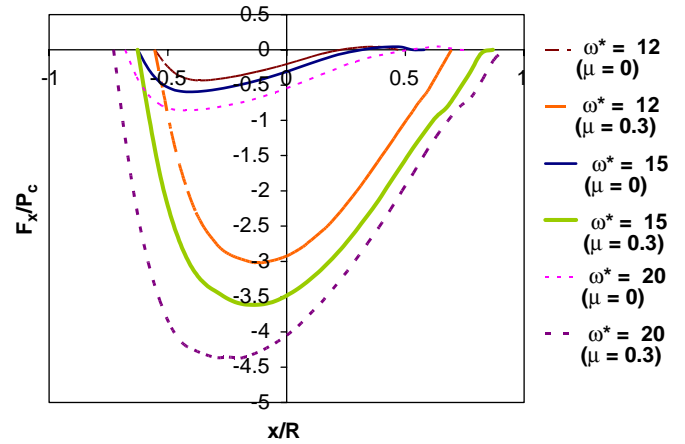


Fig. 13. Comparison of normalized horizontal reaction force plots for steel–steel sliding with and without friction.

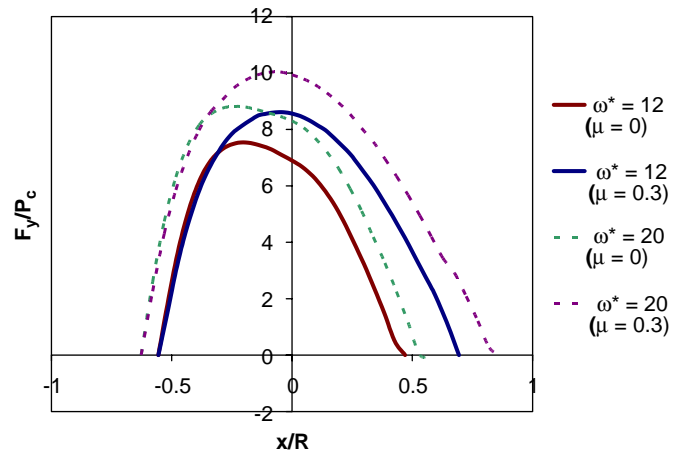


Fig. 14. Comparison of normalized vertical force plots for steel–steel sliding with and without friction.

frictional sliding, the stress field in the two sliding steel cylinders is mirrored about the horizontal contact interface. However, for frictional sliding the higher stress fields that develop during the course of sliding are tilted towards the normal to the actual plane of contact between the two cylinders. This plays an important role in the progression of yield and diminishment of the elastic core in frictional sliding. Moreover, friction also leads to the accumulation of stresses at the corners of the two cylinders as seen in Fig. 15. For high vertical interferences progressively large magnitudes of stresses are found at the base of the cylinders for both frictionless as well as frictional sliding. It is thus reasonable to postulate that for extremely high vertical interference values, these regions with such accumulation of stresses will be the cause of shearing or failure. While in the frictionless sliding case such stresses are found to develop equally at both the corners of the base of the cylinders, this is not the case when sliding is simulated in the presence of friction. For example, at  $x/R = 0$  for sliding with a vertical interference of  $\omega^* = 15$  the maximum von Mises stress,  $\sigma_e$ , at

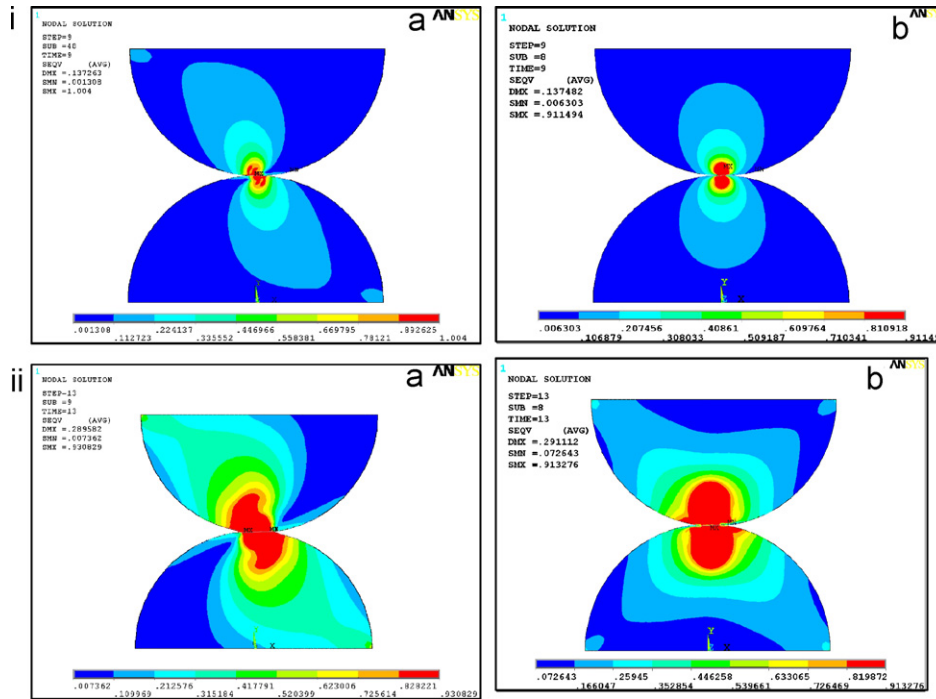


Fig. 15. von Mises stress contours for (a) frictional and (b) frictionless steel–steel sliding cylindrical contact for vertical interferences of (i)  $\omega^* = 4$  and (ii)  $\omega^* = 15$  at the vertical axis of alignment for steel–steel sliding.

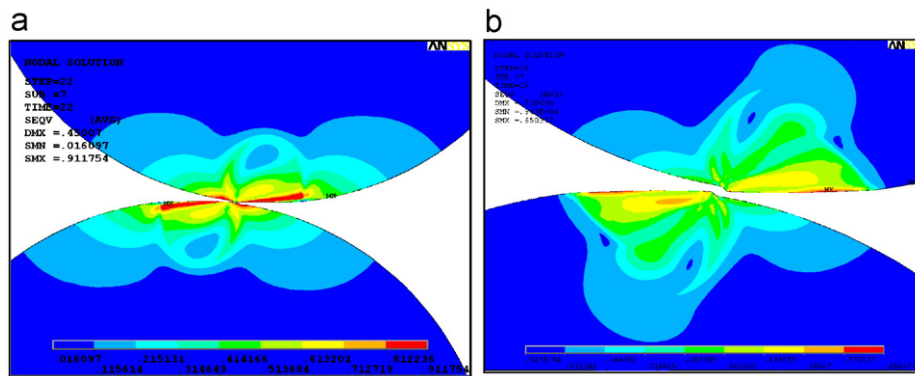


Fig. 16. Residual von Mises stress contours for (a) frictionless and (b) frictional steel–steel sliding contact for  $\omega^* = 9$ .

the base of the bottom cylinder for the frictionless sliding case is found to be 0.453 GPa. On the other hand, for sliding with friction the magnitude of  $\sigma_e$  is 0.715 GPa. This difference holds true for all the vertical interference cases, and the magnitudes of the stresses at the base of the cylinders are always higher for frictional sliding as compared to those for the frictionless sliding cases. It is notable that these stress magnitudes found at the base for both frictionless and frictional sliding are still below the yield strength; hence no yielding has occurred at these locations.

As far as the residual stresses are concerned, it is discovered that the spread is wider on the case of frictionless sliding. This can be observed by comparing residual von Mises stress contour plots shown in Fig. 16, which show the distributions for the frictionless and frictional sliding cases for a vertical interference

of  $\omega^* = 9$ . While some of the stresses are found to remain at yield value (i.e., residual plastic strain) for the frictionless sliding case, no such stress magnitudes remain after sliding is completed with friction.

### 3.6.4. Energy loss

In the absence of displacement in the vertical direction in the overall sliding process, the net energy loss purely due to plastic deformation in frictional sliding can be extracted by

$$U_{\text{net}} = U_{\text{total}} - U_{\text{friction}},$$

$$U_{\text{net}} = \int_{x_1}^{x_2} F_x dx - \mu \int_{x_1}^{x_2} F_y dx, \tag{6}$$

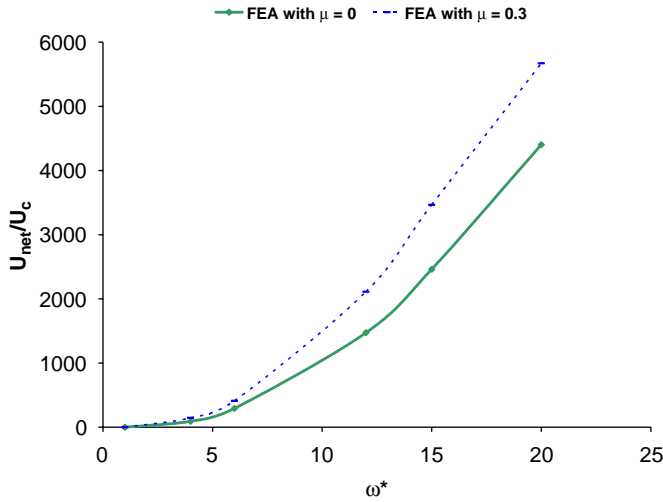


Fig. 17. Comparison of energy loss due to plasticity in frictional and frictionless steel–steel sliding.

where  $x_1$  and  $x_2$ , respectively, represent the starting and ending sliding positions of the top cylinder. Thus, energy loss due to plasticity in frictional sliding for individual preset vertical interference cases is essentially the difference between the area under the true horizontal reaction curve and the true vertical reaction plotted against the true sliding distance scaled by the coefficient of friction,  $\mu$ . The value thus obtained is called the net energy lost due to plastic deformation,  $U_{net}$ , and is normalized by  $U_c$  from Eq. (3). A second order polynomial curve is then fitted to the numerical data. It represents the trend followed by energy loss in frictional sliding for the range of the applied vertical interference,  $\omega^*$ , and is found to closely capture the increasing energy loss with increasingly elastic–plastic loading. The fitted equations are as follows:

$$\begin{aligned} \frac{U_{net}}{U_c} &= 0.690 - 2.980(\omega^* - 1) \\ &\quad + 16.991(\omega^* - 1)^2, \quad 1 \leq \omega^* \leq 6, \\ \frac{U_{net}}{U_c} &= 410.557 + 240.080(\omega^* - 6) \\ &\quad + 9.809(\omega^* - 6)^2, \quad 6 \leq \omega^* \leq 20. \end{aligned} \quad (7)$$

These equations are continuous at  $\omega^* = 6$ .

Fig. 17 shows curves representing energy loss due to plasticity in frictionless as well as frictional sliding. It is seen that the magnitudes of energy lost due to plasticity,  $U_{net}/U_c$ , are found to be consistently higher in the case of frictional sliding for the various vertical interferences in the elastic–plastic regime. Moreover, these magnitudes are seen to progressively get larger as the vertical interference increases. This observation can be attributed to the occurrence of greater plastic deformation in sliding in the presence of friction as compared to sliding without friction.

### 3.6.5. Contact half-widths

Fig. 18 shows a comparison of the contact half widths,  $b^*$ , for  $\omega^* = 12$  and 20 between frictionless and frictional sliding

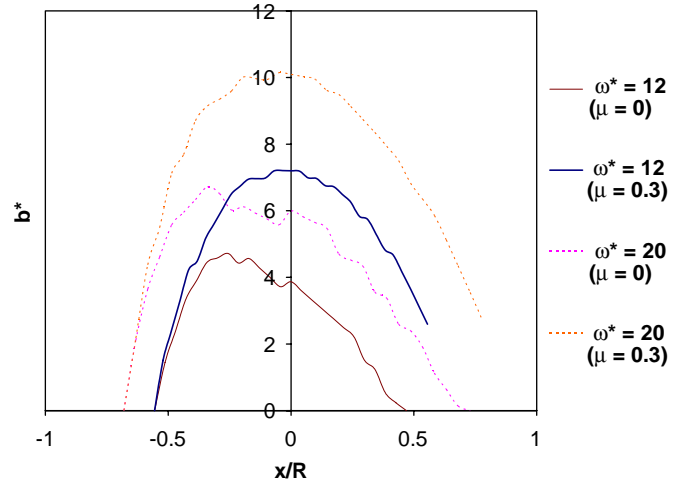


Fig. 18. Comparison of normalized contact half-width plots for steel–steel sliding with and without friction.

between two steel cylinders. It is interesting to note that the curves for frictional sliding are more or less symmetric about  $x/R = 0$ , whereas for frictionless sliding they are skewed towards the left of the vertical axis of alignment. The magnitudes of  $b^*$  for frictional sliding are found to be much larger than those for frictionless sliding.

## 4. Conclusions

This work presents the results of a FEA of sliding between two elastic–plastic bodies in cylindrical contact. The material for both the cylinders is modeled as elastic–perfectly plastic and yielding occurs according to the von Mises yield criterion. A 2D plane strain finite element model is utilized to explore the deformations, forces, stress formations, and energy losses for such frictionless sliding contact. Then a coefficient of friction of magnitude 0.3 is introduced between the two surfaces to simulate frictional sliding.

The maximum deformation at the contact interface increases with the increase in vertical interference. As sliding progresses into the unloading phase, the deformation curves flatten out at the end to signify permanent plastic deformation at the end of sliding. Significant pile-up is found in the cylinders for frictional sliding for high vertical interferences, whereas the pile-ups found after frictionless sliding for the same vertical interferences are not as pronounced.

The trends followed by the reaction forces show that more energy is invested in pushing one cylinder across the other than that restored when the cylinders are repelling each other. Also, it is established that at the point of normal contact during sliding, i.e., when the cylinders are exactly vertically aligned, the ratio of the horizontal to the vertical reaction force is not zero. Upon comparison, it is found that the horizontal reactions are much lower for sliding with friction as compared to those found in frictionless sliding. Interestingly, there is not much difference between the patterns of the vertical reactions of the two cases. By calculating the areas under the horizontal reaction

force curves for a range of vertical interferences, equations are derived to capture the energy loss due to plastic deformation in such sliding. It is discovered that there is greater energy loss due to plasticity in frictional sliding than in frictionless sliding.

It is found that for lower ranges of elasto-plastic loading, the maximum von Mises stresses arise in the region surrounding the contact interface for all cases of sliding. However, as higher vertical interferences are applied, the plastic region propagates towards the contact region and higher stresses are found to develop at the base of the cylinders. It is thus postulated that failure would occur in this region for extremely high vertical interferences even though the contact region may still yield first. This phenomenon is observed in both 2D frictional and frictionless sliding. The occurrence of such failure would be accelerated due to the presence of friction. Stress formations are symmetric about the vertical axis of alignment for steel–steel sliding for both the frictionless as well as frictional sliding. A significant observation is that while some of the residual stresses are found to be at the yield value for frictionless sliding with high vertical interferences, for frictional sliding these stresses do not quite reach the same magnitudes.

**Acknowledgment**

This research is supported in part through the Department of Defense Multidisciplinary Research Program of the University Research Initiative as Office of Naval Research Grant N00014-04-1-0601, entitled “Friction & Wear under Very High Electromagnetic Stress.” Dr. P. Peter Schmidt serves as Program Officer. Information conveyed in this manuscript does not necessarily reflect the position or policy of the Government, and no official endorsement should be inferred.

**Appendix**

This is only a concise summary of the analysis by Green [28], and the nomenclature herein is consistent with that work. Let  $x$  be the axis along the line of contact, the  $y$  axis is tangent to the two cylinders, and the  $z$  axis is the coordinate into the cylinders. Subject to normal loading the maximum (and principal) stresses occur at  $x = y = 0$ . Under a total load per unit length,  $P/L$ , maximum Hertzian pressure is generated at the origin

$$p_o = \frac{2P}{\pi bL}, \tag{8}$$

where the Hertzian half-width is given by

$$b = \left( \frac{4(\lambda_1 + \lambda_2)PR_1R_2}{L(R_1 + R_2)} \right)^{1/2} = \left( \frac{4PR}{\pi LE'} \right)^{1/2},$$

$$\lambda_i = \frac{1 - \nu_i^2}{\pi E_i}, \quad i = 1, 2, \quad \frac{1}{E'} = \frac{1 - \nu_1^2}{E_1} + \frac{1 - \nu_2^2}{E_2}. \tag{9}$$

Now defining  $\zeta = |z/b|$ , then the stresses for cylindrical contact are

$$\sigma_y = \left( 2\zeta - \sqrt{1 + \zeta^2} \left( 2 - \frac{1}{1 + \zeta^2} \right) \right) p_o, \tag{10}$$

$$\sigma_z = -\frac{p_o}{\sqrt{1 + \zeta^2}}. \tag{11}$$

These two stresses are calculated in either material 1 or 2, where only  $\zeta \geq 0$  is allowed in both materials, noting that both stresses are independent of Poisson’s ratio. Assuming the state of plain strain then the transverse stress is  $\sigma_x = \nu(\sigma_z + \sigma_y)$  which reduces to

$$\sigma_x = 2 \left( \zeta - \sqrt{1 + \zeta^2} \right) \nu p_o \tag{10}$$

The discussion is limited to the range  $0 \leq \nu \leq 1/2$ . Conveniently, letting  $\nu$  approach zero leads to a bi-axial stress state (i.e., plane stress). The maximum von Mises stress,  $\sigma_e$ , normalized by the contact pressure,  $p_o$ , is calculated by

$$\frac{\sigma_e}{p_o} = \sqrt{\frac{[1 - 2\zeta(\sqrt{1 + \zeta^2} - \zeta)][1 + 4\zeta^2 + 4(1 + \zeta^2)(\nu - 1)\nu]}{1 + \zeta^2}} \tag{12}$$

The above varies with  $\zeta$ , where  $\nu$  is a parameter. The maximum von Mises stress is obtained from  $d(\sigma_e/p_o)/d\zeta = 0$ . Defining,  $C = p_o/\sigma_{e-max}$ , results in  $C = C(\nu)$ , and the analysis of which gives the following:

$$C = \begin{cases} \frac{1}{\sqrt{1 + 4(\nu - 1)\nu}} & \zeta_m = 0 @ \nu \leq 0.1938, \\ 1.164 + 2.975\nu - 2.906\nu^2 & \zeta_m = 0.223 + 2.321\nu \\ & -2.397\nu^2 @ \nu > 0.1938. \end{cases} \tag{13}$$

This value of  $C$  is valid for as long as the material is elastic, i.e., up to yielding onset. This value is used to calculate critical parameters. The maximum deformation in a cylindrical line contact is given by

$$\omega = \frac{1}{\pi E'} \frac{P}{L} \left[ \ln \left( \frac{4\pi E' R}{P/L} \right) - 1 \right]. \tag{14}$$

Using the distortion energy (von Mises) theory to predict yielding onset, then with the aid of the definition of  $C$ , the critical values for force per unit length, interference, and half-width are derived,

$$\frac{P_c}{L} = \frac{\pi R(CS_y)^2}{E'}, \quad b_c = \frac{2R(CS_y)}{E'},$$

$$\omega_c = R \left( \frac{CS_y}{E} \right)^2 \left[ 2 \ln \left( \frac{2E'}{CS_y} \right) - 1 \right], \tag{15}$$

where  $CS_y = \min(C(\nu_1)S_{y1}, C(\nu_2)S_{y2})$  accounts for the possibility of two different material properties. The maximum potential (strain) energy per unit length that can possibly be stored

(up to the point of yielding onset) is

$$\frac{U_c}{L} = \frac{\pi(CS_y)^4 R^2}{4E'^3} \left\{ 4 \ln \left[ \frac{2E'}{CS_y} \right] - 3 \right\}. \quad (16)$$

## References

- [1] J.A. Johnson, F.C. Moon, Elastic waves and solid armature contact pressure in electromagnetic launchers, *IEEE Trans. Magn.* 42 (3) (2006) 422–429.
- [2] J. Chen, et al., Stress analysis of the human temporomandibular joint, *Med Eng. Phys.* 20 (8) (1998) 565.
- [3] G. Liu, Q.J. Wang, C. Lin, A survey of current models for simulating the contact between rough surfaces, *Tribol. Trans.* 42 (1999) 581–591.
- [4] T.R. Thomas, *Rough Surfaces*, Longman, New York, 1982.
- [5] J.A. Greenwood, A unified theory of surface roughness, *Proc. R. Soc. London A* 393 (1984) 133–157.
- [6] J.A. Greenwood, J.B.P. Williamson, Contact of nominally flat surfaces, *Proc. R. Soc. London Ser. A Math. Phys. Sci.* 295 (1442) (1966) 300–319.
- [7] J.A. Greenwood, J.H. Tripp, The elastic contact of rough spheres, *ASME J. Appl. Mech.* 34 (1967) 153–159.
- [8] C.C. Lo, Elastic contact of rough cylinders, *Int. J. Mech. Sci.* 11 (1969) 105–115.
- [9] D.J. Whitehouse, J.F. Archard, The properties of random surface of significance in their contact, *Proc. R. Soc. London A* 316 (1970) 97–121.
- [10] T. Tsukizoe, T. Hisakado, On the mechanism of contact between metal surfaces: part 2—the real area and the number of contact points, *ASME J. Lubr. Tribol.* F90 (1968) 81–90.
- [11] A.W. Bush, R.D. Gibson, T.R. Thomas, The elastic contact of rough surfaces, *Wear* 35 (1975) 87–111.
- [12] A.W. Bush, R.D. Gibson, G.P. Keogh, Strong anisotropic rough surface, *ASME J. Tribol.* 101 (1979) 15–20.
- [13] E.J. Abbot, F.A. Firestone, Specifying surface quality—a method based on accurate measurement and comparison, *Mech. Eng.* 55 (1933) 569.
- [14] D.G. Evseev, B.M. Medvedev, G.G. Grigoriyan, Modification of the elastic–plastic model for the contact of rough surfaces, *Wear* 150 (1991) 79–88.
- [15] W.R. Chang, An elastic–plastic contact model for a rough surface with an ion-plated soft metallic coating, *Wear* 212 (1997) 229–237.
- [16] Y.W. Zhao, An asperity microcontact model incorporating the transition from elastic deformation to full plastic flow, *ASME J. Tribol.* 122 (2000) 86–93.
- [17] L. Vu-Quoc, X. Zhang, L. Lesburg, A normal force–displacement model for contacting spheres accounting for plastic deformation: force-driven formulation, *ASME J. Appl. Mech.* 67 (2000) 363–371.
- [18] G.G. Adams, M. Nosonovsky, Contact modeling—forces, *Tribol. Int.* 33 (5) (2000) 431–442.
- [19] R.L. Jackson, I. Green, A finite element study of elasto–plastic hemispherical contact, *ASME Trans. J. Tribol.* 127 (2) (2005) 343–354.
- [20] F. Wang, L.M. Keer, Numerical simulation for three dimensional elastic–plastic contact with hardening behavior, *J. Tribol.* 127 (3) (2005) 494.
- [21] D. Nelias, V. Boucly, M. Brunet, Elastic–plastic contact between rough surfaces: proposal for a wear or running-in model, *J. Tribol.* 128 (2) (2006) 236–244.
- [22] G.M. Hamilton, L.E. Goodman, The stress field created by a circular sliding contact, *J. Appl. Mech.* 33 (1966) 371–376.
- [23] G.M. Hamilton, Explicit equations for the stresses beneath a sliding spherical contact, *Proc. Inst. Mech. Eng. Part C (Mech. Eng. Sci.)* 197 (1983) 53.
- [24] M. Busquet, H. Chollet, L. Baillet, C. Dagorn, J.B. Ayasse, Y. Berthier, From railway dynamics to wheel/rail contact mechanics, an approach for the modelling of the wheel/rail contact: elasto–plastic response of the railhead, *Proc. Inst. Mech. Eng. Part F (J. Rail Rapid Transit)* 220 (F3) (2006) 189–200.
- [25] A. Faulkner, R.D. Arnell, Development of a finite element model to simulate the sliding interaction between two, three-dimensional, elastoplastic, hemispherical asperities, *Wear* 242 (1) (2000) 114.
- [26] M. Nosonovsky, G.G. Adams, Steady-state frictional sliding of two elastic bodies with a wavy contact interface, *J. Tribol. Trans. ASME* 122 (3) (2000) 490.
- [27] K.L. Johnson, *Contact Mechanics*, Cambridge University Press, Cambridge, 1985.
- [28] I. Green, Poisson ratio effects and critical values in spherical and cylindrical Hertzian contacts, *Int. J. Appl. Mech.* 10 (3) (2005) 451–462.
- [29] R. Jackson, I. Chusoipin, I. Green, A finite element study of the residual stress and deformation in hemispherical contacts, *J. Tribol.* 127 (3) (2005) 484.